WFIRST/AFTA Coronagraph Contrast Performance Sensitivity Studies: Simulation versus Experiment

Erkin Sidick*, Byoung-Joon Seo, David Marx, Ilya Poberezhskiy, and Bijan Nemati
Jet Propulsion Laboratory, California Institute of Technology, 4800 Oak Grove Drive, Pasadena, CA 91109

ABSTRACT

The WFIRST/AFTA 2.4 m space telescope currently under study includes a stellar coronagraph for the imaging and the spectral characterization of extrasolar planets. The coronagraph employs sequential deformable mirrors to compensate for phase and amplitude errors. Using the optical model of an Occulting Mask Coronagraph (OMC) testbed at the Jet Propulsion Laboratory, we have investigated through modeling and simulations the sensitivity of dark hole contrast in a Hybrid Lyot Coronagraph (HLC) for several error cases, including lateral and longitudinal translation errors of two deformable mirrors, DM1 and DM2, lateral and/or longitudinal translation errors of an occulting mask and a Lyot-Stop, clocking errors of DM1 and DM2, and the mismatch errors between the testbed and the model sensitivity matrices. We also investigated the effects of a control parameter, namely the actuator regularization factor, on the control efficiency and on the final contrast floor. We found several error cases which yield contrast results comparable to that observed on the HLC testbed. We present our findings in this paper.

Keywords: Coronagraphy, adaptive optics, deformable mirrors, space telescopes, exoplanets

1. INTRODUCTION

NASA's Science Mission Directorate has begun the study phase of the WFIRST-AFTA mission [1-2], with an anticipated launch date early in the next decade. That study included a high-contrast stellar coronagraph to complement the WFIRST instrument. A series of 9 milestones were developed to demonstrate the technology readiness of the coronagraphic instrument under an aggressive schedule. This instrument is baselined to use two separate but compatible modes, a Hybrid Lyot Coronagraph (HLC) [3-6] and a Shaped-Pupil Coronagraph [7-8]. Another design is based around a Phase-Induced Amplitude Apodization Complex-Mask Coronagraph (PIAACMC) [9-10], and is being matured as a backup. Successful completion of all 9 milestones will bring the instrument to NASA Technology Readiness Level 5 (TRL-5) in September 2016.

Recently, the HLC project team at JPL has successfully completed Milestone 5, defined as "The occulting mask coronagraph (OMC) in the HCIT demonstrates 10^{-8} raw contrast with 10% broadband light centered at 550 nm in a static environment," with the OMC being the catch-all term for the combination of the HLC and the SPC in a single instrument [8]. That is, in an effort to meet the requirement of Milestone 5, a mean contrast of 8.54x10-9 was achieved in a 360-deg dark hole with a working angle between 3λ/D and 9λ/D with arbitrary polarization on the HLC static testbed. The modulated component of this contrast value is $4.09\text{x}10^{-9}$, and the unmodulated one is $4.46\text{x}10^{-9}$ [11].

The coronagraphic configuration of OMC optical model is essentially the same as that of HLC static testbed. When we included in the OMC optical chain only the measured and the estimated surface height errors of various optics, which is referred to as a "Nominal Case" in this paper, and carried out wavefront control (WFC) or electric-field conjugation (EFC) simulations, we obtained broadband contrast value that is much better than the measured one. Also, the contrast versus wavelength curve, or contrast chromaticity, obtained in simulations is relatively flat as compared to the measured curve, which exhibits an upward "U-like" shape. In other words, the contrast performance of the HLC displayed some discrepancy between the testbed and the model. In order to understand the possible causes of the observed contrast behavior of HLC, we carried out a series of WFC simulations on OMC by including either alignment calibration errors or Jacobian errors, and using different actuator regularization scheme. In most cases considered, we were able to find a combination of errors and an actuator regularization coefficient that yield contrast results comparable to those observed

*Erkin.Sidick@jpl.nasa.gov; Phone 1 818 393-7585; Fax 1 818 393-3290; www.jpl.nasa.gov

Advances in Optical and Mechanical Technologies for Telescopes and Instrumentation II, edited by Ramón Navarro, James H. Burge, Proc. of SPIE Vol. 9912, 99126M
 · doi: 10.1117/12.2231763

on the HLC testbed. In some cases, we compared the model prediction with testbed in terms of both full and half dark-hole contrast results. We present and discuss our results in this paper.

2. BACKGROUND

2.1 The OMC Optical System

The key elements of the OMC layout in the *xz*-plane is shown in Figure 1. The starlight is delivered to the OMC input pupil (Pupil-1) by a telescope. On the HLC testbed, we use a broadband light source centered at wavelength λ_c=550nm in combination with five 2%-bandpass filters whose passbands are centered at 530, 540, 550, 560 and 570nm, respectively. In simulations, we assume the input broadband light consists of 5 monochromatic light beams whose wavelengths are equal to those listed above. A pair of 48x48 actuator deformable mirrors, DM1 and DM2, is placed in series in a shared collimated beam and forms the WFC subsystem. DM1 is located near the system pupil, and DM2 in the downstream of this pupil. They provide the control of both phase and amplitude errors in the telescope. The coronagraphic subsystem is made of just two elements, a focal-plane mask (FPM) and a Lyot-Stop. The lenses represent the powered elements in the system.

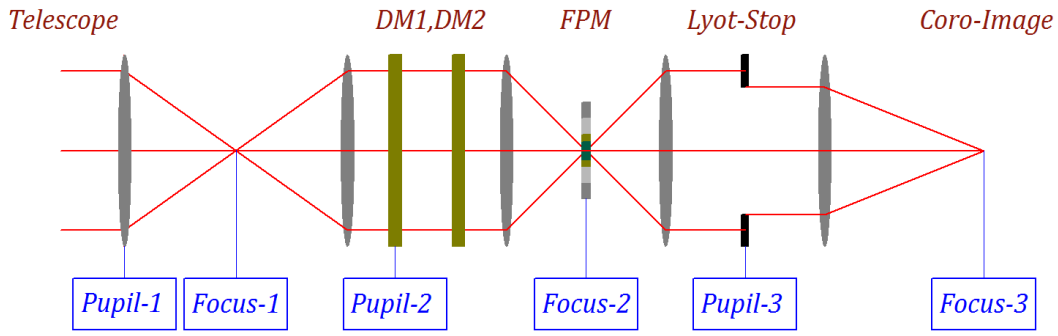

Figure 1. The key elements of the Modelable Coronagraph Testbed (OMC) layout. The light source ("starlight") is a collimated beam delivered by a telescope to input pupil (Pupil-1), and a CCD science camera is located at the coronagraphic image (Coro-Image, Focus-3) plane for detecting the image of the "starlight".

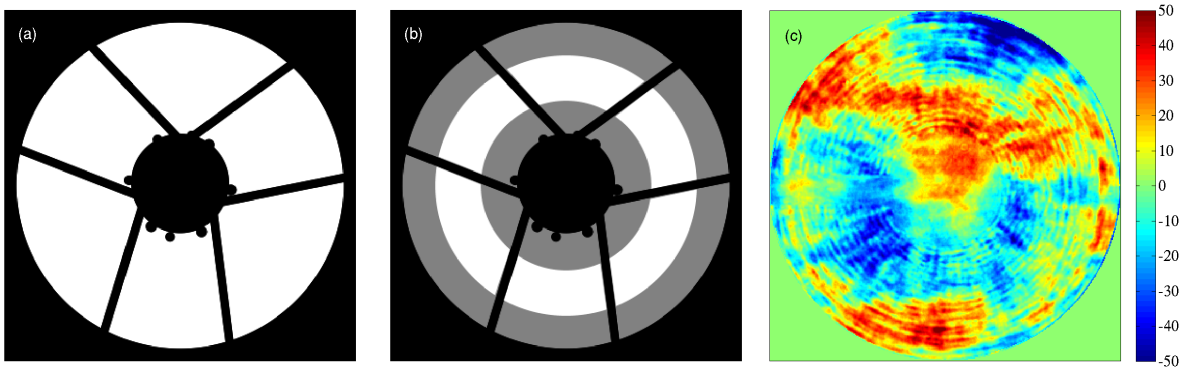

Figure 2. (a) The AFTA telescope obscuration pattern. It is the "old" pattern and includes metrology markers along the edge of the secondary obscuration. Because the primary and the secondary mirrors will be refigured and recoated, these will be removed. The HLC design simulated here is for this "old" pattern. (b) The Lyot-Stop. The AFTA pupil, as projected to the coronagraph, is shown in black, the Lyot-Stop in gray, and the pattern of the transmitted light is in white. (c) Phase error map generated by combining the measured surface height error maps of 10 optical surfaces with several other synthetic phase error maps. The latter are generated by using a PSD specification that is used in the simulations to represent optical surface fabrication errors. Each optic has a different phase or phase and amplitude error maps and WFE map in part (c) includes the phase errors of all the optics up to Lyot-Stop. The root-mean-square (RMS) and the peak-to-valley (PV) values of this WFE map are RMS = 19.1 and PV = 136.9nm, respectively.

The AFTA telescope pupil is obscured by the secondary mirror and its six support struts, as shown in Fig. 2(a). The DMs are used in combination with a focal plane or an occulting mask and a Lyot plane mask, as shown in Fig. 2(b), to generate the high-contrast dark field, as well as to correct for static optical design and manufacturing imperfections and to compensate for slow thermal drift in the telescope optics. In Fig. 2(b), the AFTA pupil, as projected to the coronagraph, is shown in black, the Lyot Stop in gray, and the pattern of transmitted light is in white. In all of our subsequent simulations, we include a "Nominal WFE map" in our model, as shown in Fig. 2(c). In our PROPER simulation software [12, 13], it is introduced into the input pupil, or Pupil-1 in Fig. 1. This error map was generated by combining two different types of phase errors. The first corresponds to the measured surface height error maps of 10 optical surfaces. The second corresponds to the synthetic phase errors produced by using a PSD specification that is used in the simulations to represent the fabrication errors of the optical surfaces whose surface heights have not been measured. The total phase error map does not exactly correspond to the testbed referenced in this study, instead, it is something we chose to represent the total phase of the testbed.

2.2 The Definitions of Normalized Intensity and Contrast

For the current optical system with two DMs, we carry out wavefront control over an annular (360-deg) dark-hole region bound by $R_{\min} = 3\lambda_c/D$ and $R_{\max} = 10\lambda_c/D$, where D~=48mm is the diameter of the input pupil aperture, $R = \sqrt{x^2 + y^2}\,/\,f$, and f is the system focal-length. We usually evaluate the contrast performance of the HLC using a normalized intensity and a contrast. The former is defined as

$$I(x, y) = I_o(x, y) / I_{uo\max}, \tag{1}$$

where $I_o(x, y)$ is the image intensity of the occulted star, and $I_{uo\max}$ is the peak value of the unocculted star intensity. It is closely related to the contrast, the metric used most commonly in the fields of high-contrast imaging. The contrast of a field is defined as the planet-to-star flux ratio when the peak pixel of the planet's point spread function (PSF) is equal to the mean per-pixel brightness of the field [13]. We will keep track the values of two metrics in this paper, the mean broadband contrast, $C_{\rm bb}$, and the mean narrowband contrast, $C_{\rm nb}$. The $C_{\rm bb}$ is the mean value of a broadband contrast map inside an annular region from $3\lambda_c/D$ to $8\lambda_c/D$. In the actual testbed, we obtain $C_{\rm nb}$ with 2% (10 nm) optical bandwidth. We ignore this bandwidth when we compare to the simulation result, where truly monochromatic light is considered. The $C_{\rm nb}$ is the same as $C_{\rm bb}$ except that the testbed $C_{\rm nb}$ is calculated from 2% narrowband contrast images and the model $C_{\rm nb}$ from the contrast images of monochromatic light. The broadband image intensity is obtained by simply averaging the narrowband or the monochromatic light intensities at 5 different wavelengths. For the nominal case, we obtain $C_{\rm bb} = 7.88\text{E}-11$ in our model. In general, the values of $C_{\rm bb}$ and $C_{\rm nb}$ are scored in a dark-hole region from $3\lambda_c/D$ to $9\lambda_c/D$. However, we limit the scoring window from $3\lambda_c/D$ to $8\lambda_c/D$ when we compare testbed and simulation results because of the testbed field stop limitation of 8.5 λ_c/D.

2.3 About the WFC Algorithm

In this paper, we use a control algorithm similar to the "minimum-wavefront and optimal control compensator" described in detail in Ref. [14]. This approach is also called "Actuator regularization" [15]. The WFC algorithm described in Ref. [14] uses the wavefront phase at the system exit pupil as its input, and calculates the actuator commands as its output. In the present case, we set the DM actuators to superpose the negative of the e-field onto the image plane, with a goal to make the image intensity zero on the dark-hole region on the image plane. Therefore, the WFC algorithm uses an e-field column-vector $\vec{\mathbf{e}}$ as its input, where

$$\vec{\mathbf{e}} = \begin{bmatrix} \Re(\vec{\mathbf{E}}) \\ \Im(\vec{\mathbf{E}}) \end{bmatrix}. \tag{2}$$

The joint cost function now becomes as

$$J = \frac{1}{2}\left(\vec{\mathbf{e}}^T\vec{\mathbf{e}} + C_{\rm wu}\vec{\mathbf{u}}^T\vec{\mathbf{u}}\right), \tag{3}$$

and the gain matrix $\widetilde{\mathbf{G}}$ is obtained from

$$\widetilde{\mathbf{G}} = \left[\widetilde{\mathbf{S}}^T\widetilde{\mathbf{S}} + C_{\mathrm{wu}}\widetilde{\mathbf{I}}\right]^{-1}\widetilde{\mathbf{S}}^T . \tag{4}$$

In Eq. (2), $\vec{\mathbf{E}}$ is the column-vector of the complex e-field on the dark-hole region, and in Eq. (3) the C_{wu} is the actuator regularization coefficient. $\vec{\mathbf{E}}$ is formed by stacking the elements of the complex e-field inside the dark-hole region in a certain order, as was explained in Eq. (1) of Ref. [14]. The $\Re(\vec{\mathbf{E}})$ and the $\Im(\vec{\mathbf{E}})$ are the real and the imaginary parts of $\vec{\mathbf{E}}$, respectively. In Eq. (4), the $\widetilde{\mathbf{S}}$ is the sensitivity matrix consisting of the influence functions of all actuators. It is also called "DM actuator response matrix" [13] and "Jacobian" [8].

When operating the HLC testbed, the operator of the testbed does not have direct access to the complex e-field in the coronagraphic image-plane. Therefore, the operator does a wavefront estimation with a pairwise estimation scheme, in which "probes" are placed on one DM to modulate the electric field across the region of interest [16, 8]. Given two or more pairs of probes, along with an image with no probes at all, both the complex e-field of the residual simulated starlight and the portion of the e-field that does not interact with the probes and hence is unlikely to be correctable can be estimated (The components that do and do not interact with the probes are referred to as the "coherent" and "incoherent" parts, or "modulated" and "unmodulated" parts, respectively). More details of the EFC algorithm and its testbed implementation are given in Refs. [15, 8].

The simulation results exclude the errors associated with the complex e-field estimation process by obtaining the complex e-field at the final focal plane directly. The simulation creates a 2048x2048-pixel e-field at the final image plane for an aperture of 336pixels across, with ~6.1 pixels per $f\lambda_c/D$. Considering only the pixels in the dark-hole and 5 wavelengths gives an e-field vector, $\vec{\mathbf{e}}$, having 32,640 field pixels at $0.3\lambda_c/D$ sampling. There are a total of 48x48x2=2304 DM actuators in the current 2-DM system, so $\widetilde{\mathbf{S}}$ has a size of 32,640 x 2304 pixels.

3. RESULTS

3.1 Nominal Case (Surface Height Errors Only) of Simulation and Measured Contrast Maps

Different researchers follow different approaches when choosing C_{wu}–values for EFC. The approach used on a testbed also differs from the one used in modeling. Our standard approach in EFC modeling is to initially start the process with a C_{wu}-value somewhat greater than a critical value, or C_{wuc}, carry out EFC for, say, about 5 iterations, then increase it by 10x and carry out EFC for another number of iterations. After that repeat the latter step for one or more times. The C_{wuc} is defined as the minimum of C_{wu} such that the EFC process does not diverge in the first EFC iteration. We find C_{wuc} by trial and error both on the testbed and in the model. In most cases of simulation, we try values such as $C_{\mathrm{wu}} = a, a\mathrm{x}10,$

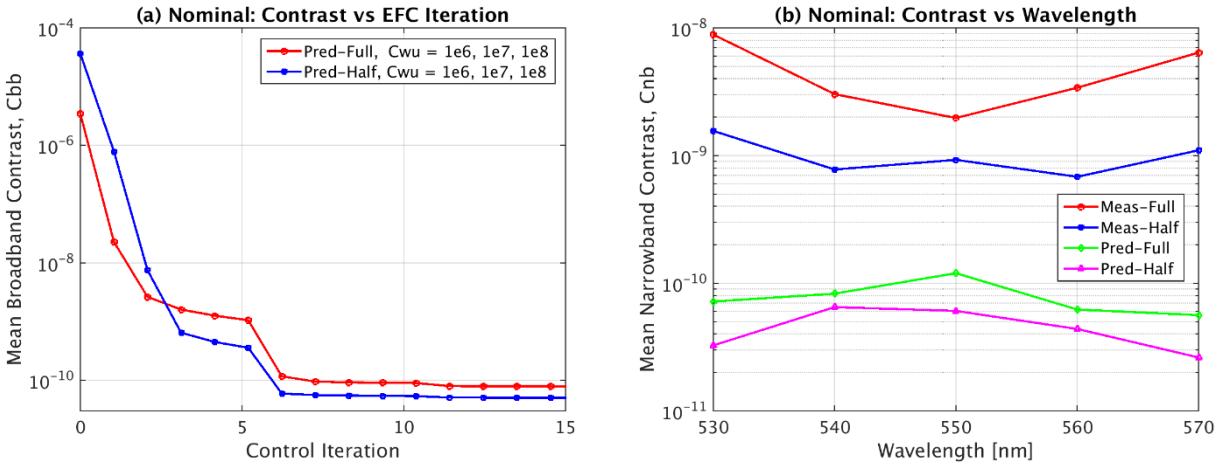

Figure 3. (a) Predicted (Pred) mean broadband contrast, C_{bb}, versus control iteration number. The word "Full" and "Half" used in the figure legends mean "full dark-hole" and "half dark-hole", respectively. The value of actuator regularization coefficient, C_{wu}, is changed after each 5 EFC iterations as listed in the figure legends. (b) Measured (Meas) and predicted chromaticity, or wavelength dependence, of mean narrowband contrast, C_{nb}. For predictions, the values of DM actuator solutions corresponding to Iteration = 15 in part (a) are used.

ax100, where a is a constant. In some cases we also carry out a finer search with $C_{wu} = a \times 3, a \times 5, a \times 7$.

For the nominal case of OMC, that is, when only the total wavefront phase error in Fig. 2(c) is included in simulation, we obtained the C_{bb} versus iteration number results shown in Fig. 3(a). In this simulation, the EFC process was started with C_{wu} = 1E6. Then, after initial 5 iterations, it was increased to C_{wu} = 1E7. And after another 5 iterations it was further increased to C_{wu} = 1E8. Such a condition is indicated in the figure legends. Carrying out EFC with three C_{wu}–values of $C_{wu} = a, a \times 10, a \times 100$ is the standard approach that we follow in our simulations.

Figure 3(b) compares the measured chromaticity of the mean narrowband contrast, C_{nb}, with the predictions. In both full and half dark-hole cases, the measured and the predicted results are very different from each other, and the predicted C_{nb} values are more than 10x better than the measured ones. The shapes of the measured and the predicted C_{nb} curves are quite different as well.

Figure 4 shows an example of narrowband normalized intensities at 5 different wavelength bands measured on our HLC testbed. The top-row results correspond to full dark-hole from 3 to 9λ_c/D, and the bottom-row to the right half dark-hole. The dark-hole images like the ones shown in Fig. 4 are very repeatable, and we chose to use these ones as our testbed results for the purpose of comparison. More detailed information about the HLC testbed and the measurement method used can be found in Ref. [5].

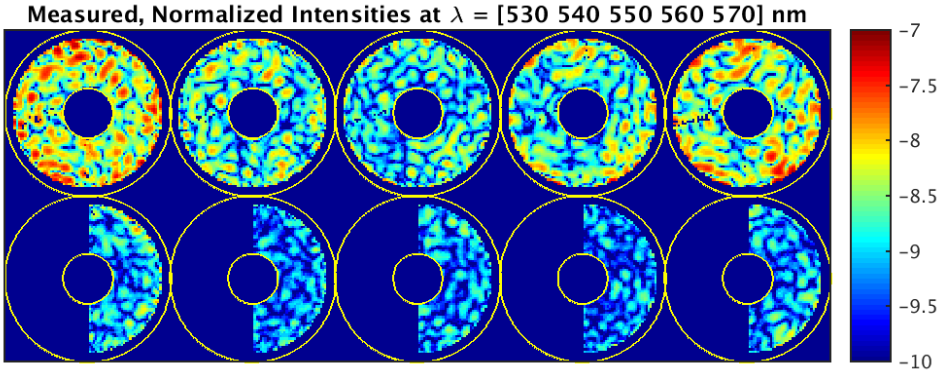

Figure 4. An example of measured normalized intensity, $I(x,y)$, inside the 3 – 9λ_c/D dark-hole region. The boundaries of the dark-hole area are indicated by two yellow-circles. The 5 intensity maps correspond to five 2% narrowbands centered at 530, 540, 550, 560 and 570nm, respectively. The top-row is the example of full dark-hole intensity maps, and the bottom-row is the half dark-hole ones.

3.2 Nominal Plus Alignment Calibration Errors

We have seen in the previous sub-section that the OMC model predicts much better contrast values relative to the testbed results when only the nominal phase errors are included in the simulations. In order to gain some understanding on the possible causes of testbed contrast performance, we carried out a series of simulations by including different types of errors in our model. The first case we considered is the 400um lateral translation of DM2 in the negative x-direction. We call this error as "DM2-Tx = -400um". The OMC and the HLC optical chains sit on the xz-plane, thus this error corresponds to an in-plane translation of DM2 perpendicular to the beam direction.

If we start the EFC with a C_{wu}–value close to C_{wuc} (Smaller C_{wu}-values), we obtain the predicted contrast chromaticity results shown in Fig. 5(a). In this case, the predicted contrast curves do not match with the measured ones. However, if we choose less aggressive or non-optimum C_{wu}-values (Larger C_{wu}-values), we can greatly improve the agreement between the measurement and the model prediction, as shown in Fig. 5(b).

Figure 6 shows the predicted normalized intensity maps corresponding to the case of Fig. 5(b). They qualitatively look fairly similar to the measured ones in Fig. 4.

Even though the agreements between the predicted and the measured contrast results are fairly good in Fig. 5(b) and Fig. 6, it is in general less likely that the degradation in observed contrast is caused by a single source of errors, such as the

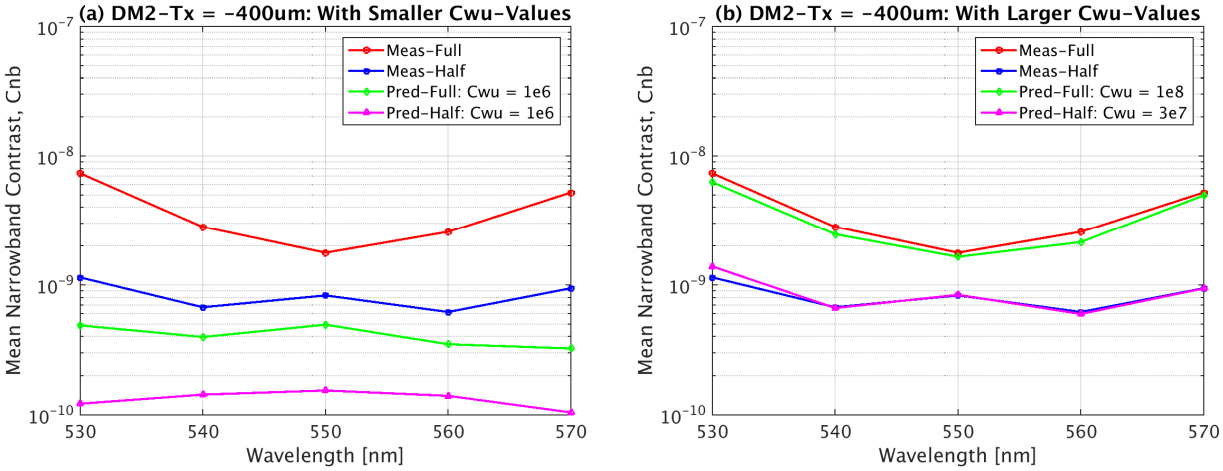

Figure 5. (a) Measured (Meas) and predicted (Pred) wavelength dependence of mean narrowband contrast, C_{nb}, when DM2 is shifted laterally in the negative x-direction by 400um (DM2-Tx = -400um). The results of both full and half dark-holes were obtained with C_{wu} = [1e6 1e7 1e8]. (b) Same as part (a), except that results of full dark-hole were obtained with C_{wu} = [1e8 1e9 1e10], and those of half dark-hole with C_{wu} = [3e7 1e8 1e9].

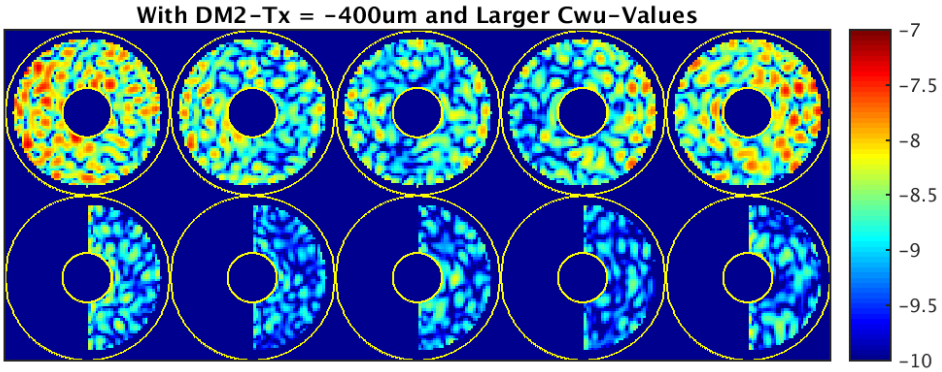

Figure 6. Predicted normalized intensity, $I(x,y)$, inside the 3 – 9λ_c/D dark-hole region corresponding to the error case of DM2-Tx = -400um. The boundaries of the dark-hole area are indicated by two yellow-circles. The 5 intensity maps correspond to five monochromatic light beams at 530, 540, 550, 560 and 570nm, respectively. The top-row shows the full dark-hole intensity maps, and the bottom-row shows the half dark-hole ones.

Table 1. Names of the optical elements and the values of misalignment errors included in the simulations of sub-section 4.3. "Lyot" means Lyot-Stop, and "Occ" means the focal-plane occulting mask. "Tx" is x-translation, and "Rz" is z-rotation.

	Name	8-Errors	11-Errors	Unit
DM1	Tx	100	109	um
	Ty		32	um
	Rz	0.2	-0.51	deg
DM2	Tx		71	um
	Ty	-100	-17	um
	Rz	-0.2	-1.06	deg
Lyot	Tx	100	105	um
	Ty	50	34	um
Occ	Tx	2	0.3	um
	Ty	-2	3.0	um
	Tz		111	um

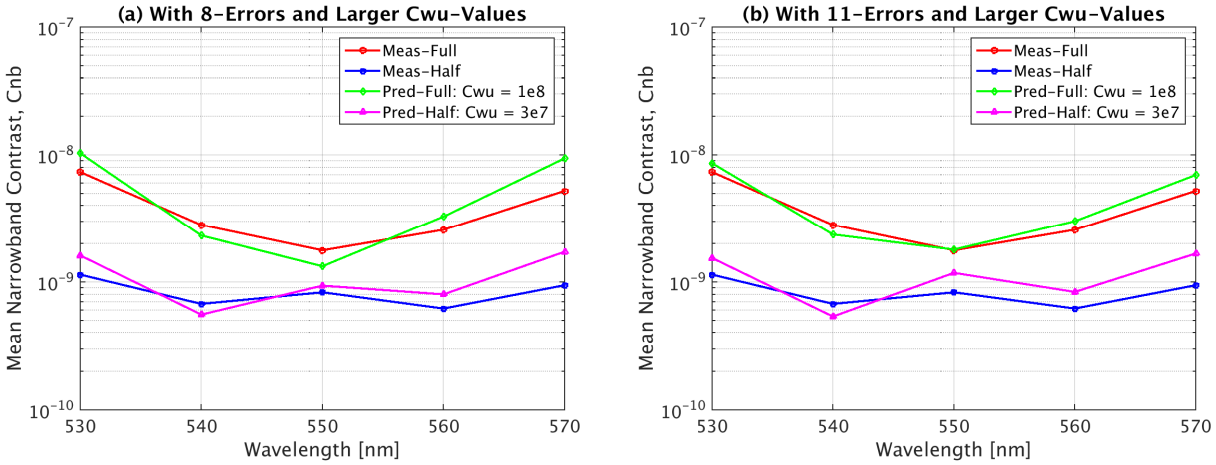

Figure 7. (a) Measured (Meas) and predicted (Pred) wavelength dependence of the mean narrowband contrast, C_{nb}. when 8 optical element misalignment errors are included. The names of the optical elements and the values of their errors are listed in Table 1. The predicted results of full dark-hole were obtained with C_{wu} = [1e8 1e9 1e10], and those of half dark-hole with C_{wu} = [3e7 1e8 1e9]. (b) Same as part (a), except that 11 optical element misalignment errors are included in these simulations. The C_{wu}-values used are the same as in part (a).

lateral misalignment of DM1 or DM2. Also, the DM1 and the DM2 misalignment uncertainty is estimated to be up to ±100um, not ±400um as assumed in the above simulations. We extended the above simulations to multiple errors sources, namely, to 8 and 11 optical element misalignment errors, as listed in Table 1. The corresponding mean narrowband contrast chromaticity results are shown in Figs. 7(a-b). Again, the values and the shapes of the predicted C_{nb} curves are fairly comparable to the measured ones. The R_z-values of DM1 and DM2 are estimated to be less than 0.1deg on the HLC testbed, so the R_z-values used in the current simulations are over-estimated. But the other error values can be assumed to be within practical limits. In Table 1, the values of 8 errors were chosen directly by ourselves, but those of 11 errors were obtained through a series of Monte-Carlo simulations.

3.3 Errors in Sensitivity Matrix or Jacobian Errors

Wavefront correction is done with the electric field conjugation (EFC) algorithm as discussed in Sec. 2.3. EFC chooses DM settings to minimize the modulated part of the electric field across the dark hole based on a model of the coronagraph. Any discrepancy between the model and the testbed degrades the EFC efficiency and testbed contrast performance.

In order to find and quantify the model and the testbed mismatch in the HLC testbed [5], we carried out "Jacobian survey" by measuring the sensitivity matrix, which is the differential complex e-field per a unit actuator stroke. The sensitivity matrix serves as a set of basis functions for EFC as explained in Sec. 2.3.

We considered all of the actuators used for control, or "active actuators", for this survey. They are 1441 and 1431 actuators for DM1 and DM2, respectively, as shown in Figs. 8(a,b). The poking delta voltages shown in those figures are pre-computed using the model to have a mean $|\Delta E|^2$ value approximately equal to 1E-8. Actuators behind the Lyot Stop are poked relatively less because their resulting $|\Delta E|$ values in the dark hole are smaller than those of the actuators located in the Lyot Stop open area. A total of seven probe images taken at the center wavelength of 550 [5] are used to estimate the complete e-field per actuator [5]. It took about 2.5 minutes per actuator, and the total measurement time was approximately a week. The contrast level did not stay the same during the measurement due to drift, therefore, we performed intermittent EFC to maintain the contrast level below 1E-8.

Figures 9(a,b) show the real and the imaginary parts of the measured differential e-field generated with one actuator, Act(35,15), of DM1, the actuator located at row = 35 and column = 15 when Act(1,1) is at the lower-left corner. Figure 9(c) is the corresponding spectrum of that field. The corresponding model results are shown in Figs. 9(d-f). The delta poking voltage is 272mV in this case. In order to quantify the agreement between the measured and predicted e-fields, we use the following three metrics: (1) gain errors, (2) e-field phase piston errors and (3) e-field phase slope errors.

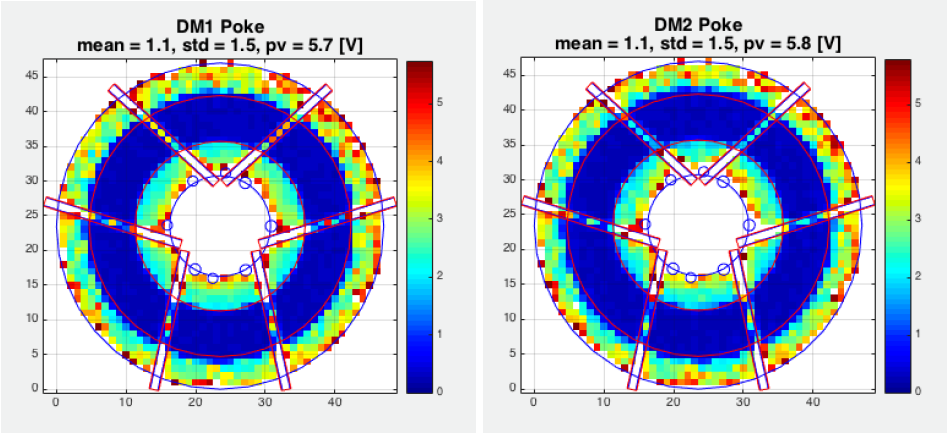

Figure 8. The poking delta voltages for DM1 and DM2 used in the Jacobian survey. They are pre-computed using the model to have a mean $|\Delta E|^2$ approximately equal to 1E-8. A total of 1441 and 1431 actuators are studied for DM1 and DM2, respectively.

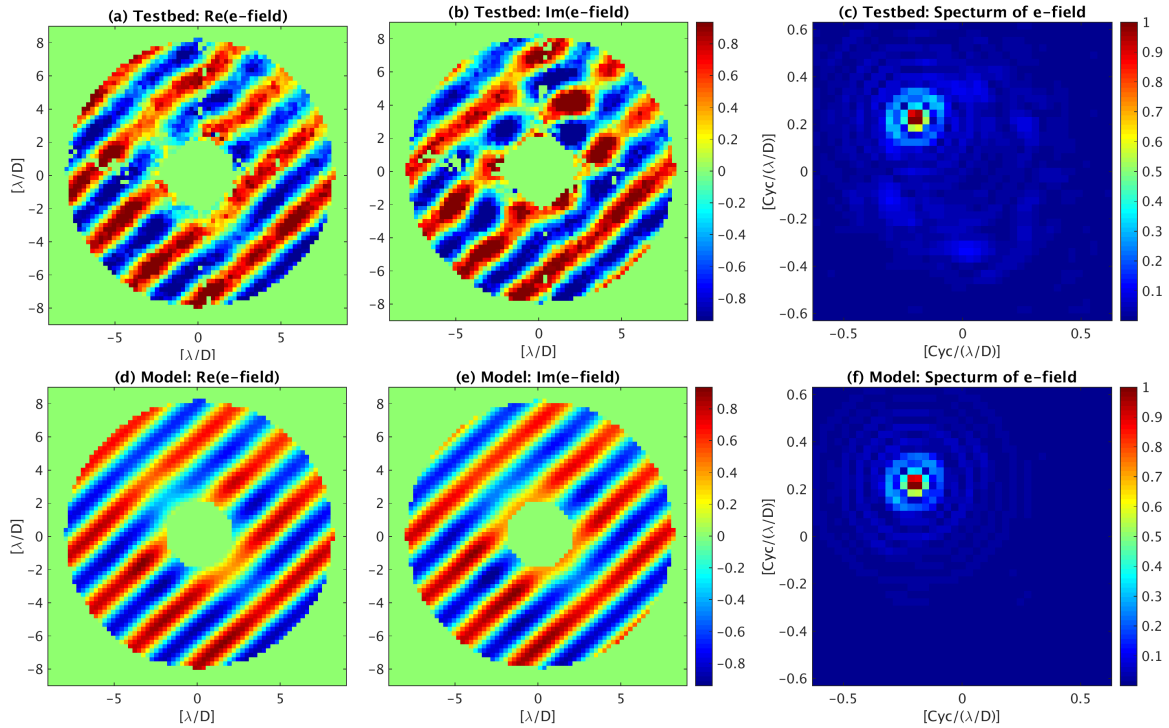

Figure 9. The real (a) and the imaginary (b) parts of the measured differential e-field at the final image-plane generated with Act(35,15) of DM1, the actuator located at row = 35 and column = 15 when Act(1,1) is at the lower-left corner, and the corresponding spectrum (c) of that field. Parts (d-f) show the corresponding model results. Only the portion of the e-field inside a $2 - 8\lambda_c/D$ annular region as shown here is considered in the current analysis.

The gain errors, shown in Figs. 10(a,b) for DM1 and DM2, are the ratio of RMS of the measured differential e-field to that of the predicted one. In a perfectly calibrated model, the gain errors are equal to one for all actuators. The gain error is caused by DM gain calibration errors, Lyot-Stop positioning errors near the Lyot-Stop mask edges, and actuator influence-function errors, *etc.* As is seen in Figs. 10(a,b), the gain errors are relatively worse near the Lyot-Stop edge or near the AFTA pupil struts. We believe this is due to a mismatch between the testbed and the model on the Lyot-Stop edge location since we could improve the gain errors locally when we move around the Lyot-Stop in the model by approximately 400 um in a 47 mm pupil. As we discuss later in this section, this error is not the major factor limiting the HLC contrast performance.

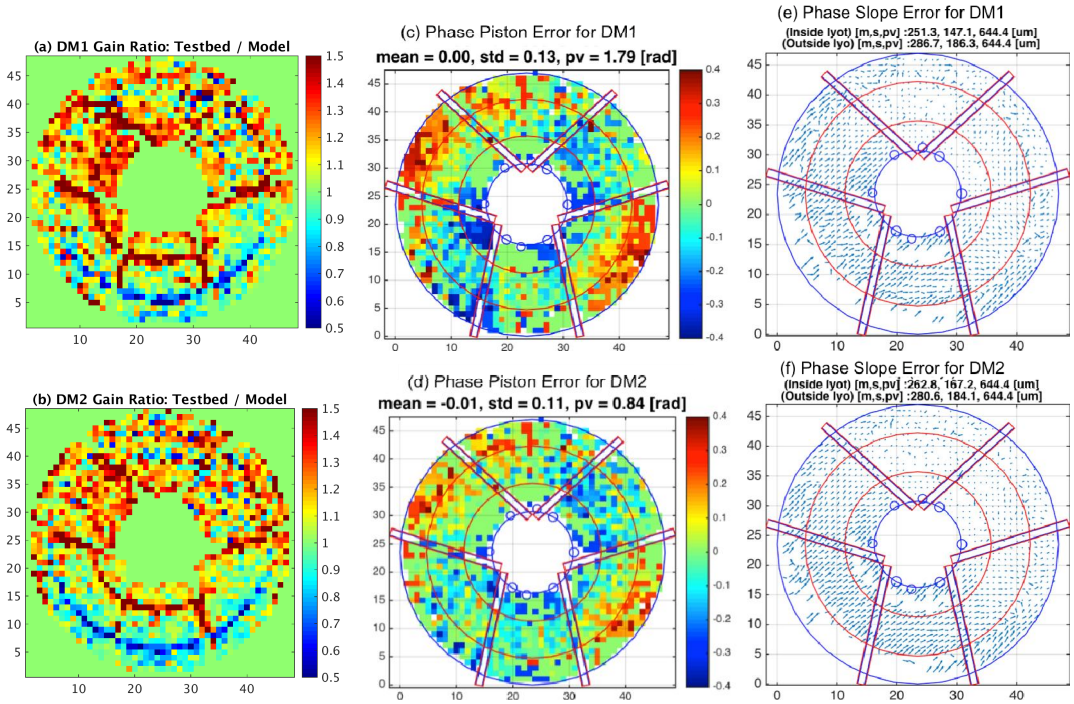

Figure 10. Testbed-to-model differences obtained in the Jacobian Survery: (a,b) Gain errors for DM1 and DM2, calculated from the ratios of the differential e-field amplitude RMS values. (c,d) Phase piston errors for DM1 and DM2, calculated from the phase piston differences in radians. (e.f) Phase slope errors for DM1 and DM2, calculated from the 2-D spatial frequency differences between modeled and measured e-fields. (e,f) are auto-scale quiver plots and their titles show the mean, standard deviation and peak-to-valley inside and outside Lyot-Stop area in unit of microns for 47mm pupil aperture diameter. See texts for more details.

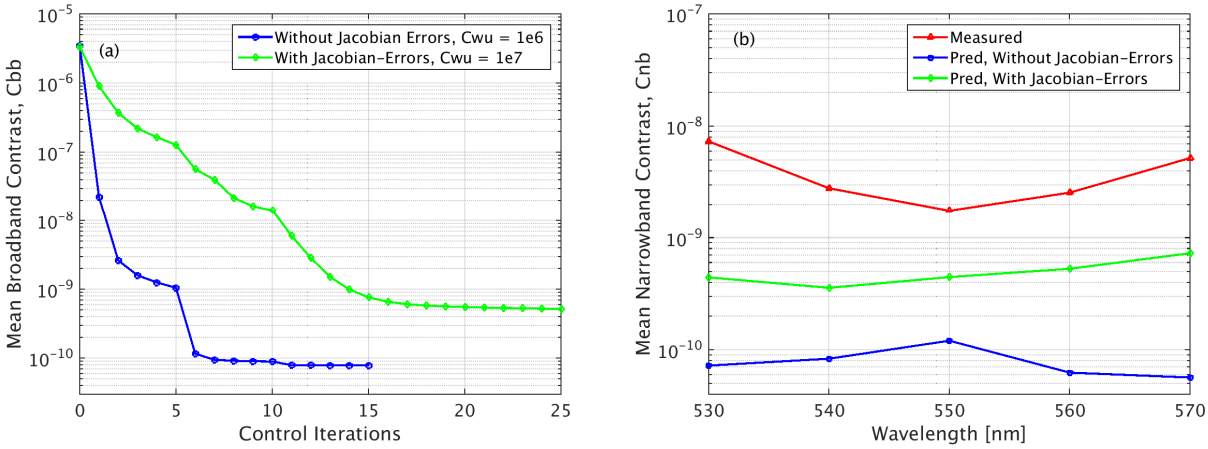

Figure 11. (a) Predicted full dark-hole mean broadband contrast, C_{bb}, versus control iteration number. The blue-curve is the same as the red-curve in Fig. 3(a) and was obtained without including the actuator Jacobian errors in the simulation. Whereas in the case of green-curve, the three kinds of the actuator Jacobian errors are included in the simulation. C_{wu} = [1e6 1e7 1e8] and C_{wu} = [1e7 1e8 1e9] in the cases of blue- and green-curves, respectively. They are close to the optimum values. (b) Measured and predicted chromaticity, or wavelength dependence, of the full dark-hole mean narrowband contrast, C_{nb}. The predicted results correspond to the two cases in part (a).

The e-field phase piston errors shown in Figs. 10(c,d) are the shifts of the fringes of the predicted e-fields relative those of the measured ones, measured in a direction perpendicular to the fringe direction, see Fig. 9. They are caused by the actuator piston offsets, or the wavefront errors, that are not captured in the model. If we examine the amplitude and the

phase plots instead of the real part and the imaginary part plots (not shown here), the e-field phase piston error shows up as a phase piston. Note that Figs. 10(c,d) have units of radians. We observe astigmatic WFE in the order of 0.11 and 0.13 radians for DM1 and DM2, respectively. We believe this is WFE calibration error in the model.

The e-field phase slope errors, shown in Figs. 10(e,f), are the 2-dimentional (2-D) spatial frequency difference between the predicted and the measured fringes. For the actuators inside the Lyot-Stop, these frequency shifts are caused by the 2-D actuator registration errors. For the actuators outside the Lyot-Stop, the Lyot-Stop edge calibration becomes a problem. Figures 10(e,f) are the 2-D quiver plots for DM1 and DM2, which are automatically scaled for the purpose of illustration here. Their mean offsets are computed to be about 250 um for the 47 mm pupil. More statistical numbers are given in the captions of Figs. 10(e,f). The 250 um mean offsets are somewhat larger than our estimate of about 100 um obtained when we register the DM actuators for building the model. Therefore, this large frequency offset errors is a problem that we could not resolve at this moment.

We carried out EFC simulations by taking into account the above 3 types of actuator Jacobian errors with near optimum C_{wu}–values for full dark-hole region, and compared the obtained contrast results with the nominal one in Fig. 11(a). As expected, the actuator Jacobian errors degrade both the EFC efficiency and the achievable contrast floor. However, as is seen from Fig. 11(b), the actuator Jacobian errors alone cannot explain the contrast floor and the contrast chromaticity observed on the testbed. In other words, we believe the observed contrast performance of the HLC is not captured by the Jacobian survey results alone.

3.4 Effects of the Actuator Regularization Coefficient

The final contrast floor achievable after each EFC session strongly depends on the value of the actuator regularization coefficient, C_{wu}. This is true in both modeling and experiment. For example, Figure 12(a) shows C_{bb} as a function of C_{wu} after the first EFC iteration. Intuitively, it is reasonable to think that letting the control program perform a C_{wu}–scan at each EFC iteration step and select the DM solutions that give the best or the smallest C_{bb}–value would make the control process easy and yield the optimum contrast. But in reality that is not case, as shown in Fig. 12(b), where the green-curve is the same as in Fig. 11(a) and blue-curve was obtained with the above-mentioned "Automatic C_{wu}" approach. That is, the EFC converges faster at the beginning when using the "Automatic C_{wu}" method, but stops at a much larger C_{bb}–level as compared the "Pre-selected C_{wu}" approach.

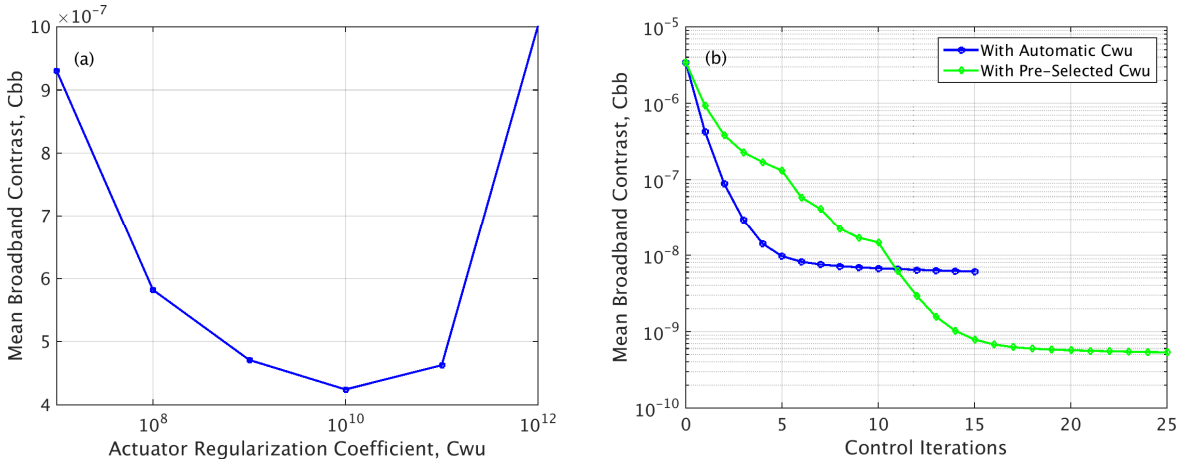

Figure 12. (a) Predicted full dark-hole mean broadband contrast, C_{bb}, versus actuator regularization coefficient, C_{wu}, corresponding to the first EFC iteration. (b) Predicted full dark-hole C_{bb} versus control iteration number. The green-curve is the same as the green-curve in Fig. 11(a) and was obtained with pre-selected C_{wu} = [1e7 1e8 1e9], whereas the blue-curve is obtained with "Automatic C_{wu}" by evaluating C_{bb} with different C_{wu}–values at each EFC iteration and selecting the DM solutions that yield the best or smallest C_{bb} –value. The three-kinds of Jacobian-errors are included in the simulations of both parts (a) and (b).

Figure 13(a) shows the C_{bb} as a function of EFC iteration number when only one C_{wu}–value is used in each EFC session, and Fig. 13(b) shows the corresponding C_{nb} versus wavelength curves. The EFC does not converge after Iteration = 6 when C_{wu} =1e7, so the C_{nb} vs wavelength curve was omitted for this case. As is seen from these results, there is an optimum C_{wu}-value when only one C_{wu}–value is used in each EFC session, and such an optimum value is much larger than the critical value. The three kinds of "Jacobian-errors" discussed in the previous section are included in all the simulations presented here.

As is seen from Fig. 13(b), the C_{nb} does not change much with wavelength when the dark-hole is not deep enough, or when the achieved contrast floor is off a lot from the optimum, as is seen from the green-curves in Figs. 13(a,b). It also becomes less dependent on wavelength when the contrast nears its optimum floor, as are seen from the pink-curves in those two plots.

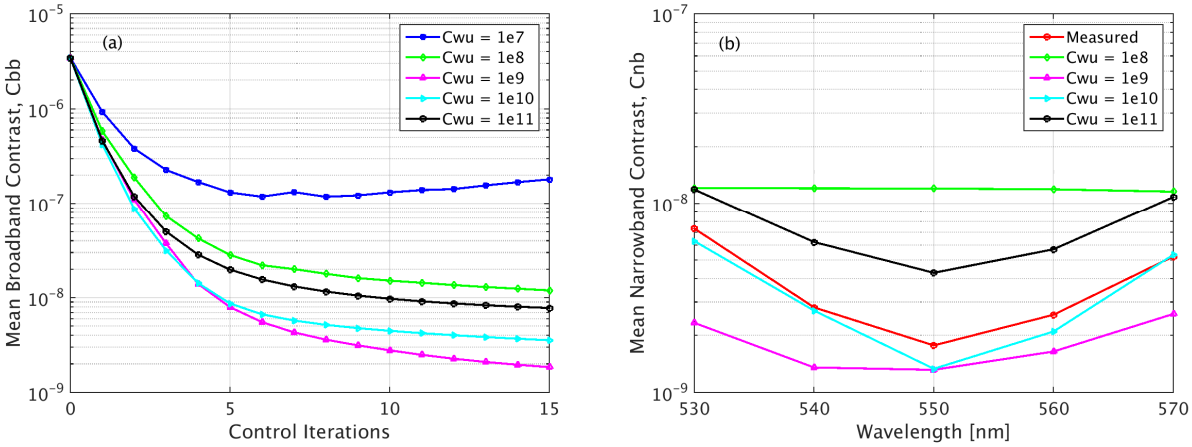

Figure 13. (a) Predicted full dark-hole C_{bb} versus control iteration number when only one C_{wu}–value is used in each EFC session. (b) Measured and predicted wavelength dependence of the full dark-hole mean narrowband contrast, C_{nb}. The four predicted curves correspond to the four cases in part (a).

4. CONCLUSION

The hybrid Lyot coronagraph (HLC) testbed at JPL has completed Milestone 5 with a mean, 10%-broadband total (modulated plus unmodulated) contrast value of 8.54E-9 at a center wavelength of 550nm in a 360deg dark-hole region covering 3 – 9λ_c/D field angle. The measured contrast versus wavelength curve exhibited an upward "U-like" shape, a result not predicted by the HLC model under a nominal error condition. In order to gain some understanding about the possible causes of the observed broadband contrast performance of HLC, we carried out a series of simulations by including different kinds of alignment errors of optical elements and sensitivity matrix errors. In several cases considered, the model predicted contrast curves agreed well with the measured ones. In some of those cases, the assumed alignment errors are within the estimated alignment uncertainty.

A "Jacobian survey" was conducted on the HLC testbed at JPL, which revealed the following three kinds of model-to-testbed mismatch errors in terms of differential e-fields: (1) Amplitude differences, (2) field shifts (or phase shifts), and (3) ripple period differences (or non-zero phase slopes). When included in simulations, these errors degraded the achievable contrast floor, but did not result in a contrast chromaticity similar to what was observed on the testbed. In other words, the Jacobian errors alone could not explain the broadband contrast behavior observed on the HLC testbed.

In addition to the alignment errors and the Jacobian errors, we have shown that the value of actuator regularization coefficient, C_{wu}, also greatly influences the achievable contrast performance of the HLC. Among the several C_{wu}–selecting approaches investigated, the "Pre-selected C_{wu}" approach worked the best in EFC simulations. But the C_{wu} –selection method that has been thus far followed on the HLC testbed is different from that approach. Therefore, investigating the C_{wu} –selection approach used on the testbed carefully, determining if the "old approach" is optimum or not, and, if it is not, then identifying the optimum one are some of the important tasks being planned for our future studies.

The research was carried out at the Jet Propulsion Laboratory, California Institute of Technology, under a contract with the National Aeronautics and Space Administration.

REFERENCES

[1] D. Spergel *et al*, Wide-field Infrared Survey Telescope-Astrophysics Focused Telescope Assets WFIRST-AFTA Final Report, http://wfirst.gsfc.nasa.gov/science/sdt_public/WFIRST-AFTA_SDT_Final_Report_Rev1_130523.pdf (2013).
[2] Ilya Poberezhskiy *et al*, "Technology development towards WFIRST-AFTA coronagraph," Proc. SPIE 9143, 91430P (2014).
[3] *John Trauger, Dwight Moody, Brian Gordon*, "Complex apodized Lyot coronagraph for exoplanet imaging with partially obscured telescope apertures," Proc. SPIE 8864, 886412 (2013).
[4] John Krist, "End-to-end numerical modeling of AFTA coronagraphs," Proc. SPIE 9143, 91430V (2014).
[5] Byoung-Joon Seo, *et al*, "Hybrid Lyot coronagraph for wide-field infrared survey telescope-astrophysics focused telescope assets: Occulter fabrication and high contrast narrowband testbed demonstration," metrics," J. Astron. Telesc. Instrum. Syst. 2(1), 011019 (2015).
[6] John Trauger, Dwight Moody, John Krist, and Brian Gordon, "Hybrid Lyot coronagraph for WFIRST-AFTA: coronagraph design and performance metrics," J. Astron. Telesc. Instrum. Syst. 2(1):011013 (2016).
[7] A. Carlotti, N.J. Kasdin, and R. Vanderbei, "Shaped pupil coronagraphy with WFIRST-AFTA," Proc. SPIE 8864, 886410 (2013).
[8] Eric Cady, *et al*, "Demonstration of high contrast with an obscured aperture with the WFIRST-AFTA shaped pupil coronagraph," J. Astron. Telesc. Instrum. Syst. 2(1):011004 (2015).
[9] Olivier Guyon, "Imaging Earth-like planets around late-type stars with low-inner working angle PIAA coronagraphy," Proc. SPIE 8864, 886414 (2013).
[10] Brian Kern, *et al*, "Phase-induced amplitude apodization complex mask coronagraph mask fabrication, characterization, and modeling for WFIRST-AFTA," J. Astron. Telesc. Instrum. Syst. 2(1):011014 (2016).
[11] Eric Cady, *et al*, "Milestone 5 Final Report: Hybrid Lyot and Shaped Pupil Broadband Contrast Testbed Demonstration for WFIRST-AFTA," http://wfirst.gsfc.nasa.gov/science/sdt_public/wps/references/WFIRST_CGI_Milestone5_Final_Report.pdf.
[12] Erkin Sidick, and F. Shi, "Effect of DM actuator gain errors on the WFIRST/AFTA coronagraph contrast performance," Proc. SPIE, vol. 9605, pp. 9505-5, August 2015.
[13] John Krist, Bijan Nemati, and Bertrand Mennesson, "Numerical modeling of the proposed WFIRST-AFTA coronagraphs and their predicted performances," J. Astron. Telesc. Instrum. Syst. 2(1):011003 (2016).
[14] Erkin Sidick, Scott A. Basinger, and David C. Redding, "An improved wavefront control algorithm for large space telescopes," Proc. SPIE, **7015**, 70154P (2008).
[15] Amir Give'on *et al*, "Broadband wavefront correction algorithm for high-contrast imaging system," Proc. SPIE, **6691**, 66910A (2007).
[16] A. Give'on, B. D. Kern, and S. Shaklan, "Pair-wise, deformable mirror, image plane-based diversity electric field estimation for high contrast coronagraphy," Proc. SPIE 8151, 815110 (2011).